Continuous Aerosol Photopolymerization to Coat De-agglomerated Nanoparticles

Hamed Nasri Lari, Jamal Chaouki, Jason R. Tavares[1]

Department of Chemical Engineering, Polytechnique Montreal, Montreal, QC, Canada H3C 3A7

Highlights

- De-agglomerated nano-TiO_2 was coated with PMMA-like film using aerosol photopolymerization.
- Presence of an PMMA-like film was confirmed by TEM, TGA, FTIR and XPS.
- Jet impactor-assisted fluidized bed reduces the size of nano-TiO_2 agglomerates.
- Coated nano-TiO_2 showed an enhanced long-term dispersibility in non-polar media.

Abstract

A novel continuous aerosol photopolymerization technique to coat nanoparticles that have been previously de-agglomerated is presented. After de-agglomeration in a jet-impactor assisted fluidized bed, monomer vapors are condensed onto the surface of aerosol nanoparticles via heterogeneous condensation. Photopolymerization is initiated through exposure to UV light. To demonstrate the process, titanium dioxide (TiO2) and methyl methacrylate (MMA) were selected as nanoparticle and organic monomer, respectively. We demonstrated this light-based technique, operated at ambient pressure and room temperature, is able to graft a PMMA-like film with a thickness of 1.5 nm on the surface of nanoparticles, confirmed by TEM and FTIR. XPS analysis confirmed formation of covalent bonds with the TiO_2 surface, indicating a surface-initiated photopolymerization. Particle size measurements in suspension state illustrated the efficiency of the de-agglomeration and subsequent coating process, as coated particles remained smaller than bare particles. UV-Vis absorbance spectra show that the coating facilitates dispersion in non-polar solvents. Finally, long-term stability experiment

---

[1] Corresponding author: jason.tavares@polymtl.ca

confirmed the suspension stability is enhanced not only because of the reduction of agglomerate sizes, but also as a result of the carbon coating which improves the interfacial interactions between particle-particle and particle-solvent. This technique can be easily combined with any continuous inorganic nanoparticle synthesis processes as a solvent-free post-synthesis process to impart a functional coating.

Keywords nanoparticle, coating, aerosol, photopolymerization, continuous, Photo-initiated Chemical Vapor Deposition (PICVD)

1. Introduction

Inorganic nanoparticles are among the most widely studied nanomaterials given their uses in a broad range of fields such as electronic, catalysis, drug delivery, sensors, cosmetics, pharmaceutical equipment, and air/water remediation. Tailoring nanoparticles for specific applications through their surface treatment has been the focus of vast research in the past two decades [1-7].

Bare metal and metal oxide nanoparticles tend to agglomerate or aggregate during their synthesis, storage or process as a result of their high surface energy and exceedingly high interparticle forces (e.g. van der Waals forces). Traditionally, surfactants are used to prevent the agglomeration of nanoparticles and improve their dispersibility through different mechanisms such as steric stabilization, electrostatic stabilization, or passivation. Despite the efficiency of surfactants, they suffer from poor thermal stability [8]. This inhibits their application in high temperature processes such as nanofluids, nanocomposites and thermoset polymers [9, 10]. To overcome this issue, coating with a thin film or passivating nanoparticles is of key importance to facilitate their handling, whilst retaining their unique, size-driven properties. On top of reducing surface energy through passivation, coating allows us to tune surface properties for specific applications. For example, coating can enhance dispersion, which is a key factor in the production of nanocomposites. Poor performance in polymer nanocomposites has been directly related to weak polymer-nanoparticle interaction, as compared to strong particle-particle interactions that drive agglomeration [11].

Nanoparticle surface functionalization with chemical groups that have affinity to the host media (e.g. polymer matrix) has shown promise in multiple fields: encapsulation of iron oxide nanoparticles with carbon chains enhances dispersion in non-polar media [1], encapsulating zirconia and alumina nanoparticles with high molecular weight polyethylene enhances the performance of nanocomposites

[12], coating silver nanoparticle with polyacrylic acid improves the preparation of silver-polymer nanocomposites [13], functionalizing hydrophobic nanoparticles with amphiphilic polymers make them compatible with biological application [14], and chemical modification of graphite nanoplates with 1,3 dipolar cycloaddition enhanced the stability of dispersion and delayed re-agglomeration in polypropylene matrix [15], to name only a few.

Traditionally, nanoparticle coating methods are categorized into wet and dry techniques. Wet methods include sol-gel, emulsification, and solvent evaporation processes [16]. Dry methods consist of physical (physical vapor deposition) and chemical (plasma-enhanced [17], thermally-activated [18], and photo-initiated chemical vapor deposition [19-21]) approaches. Physical methods coat a surface without forming of covalent bonds with the substrate, whereas chemical approaches promote bonding with free sites on the nanoparticle surface via strong covalent bonds. While several solvent-free methods have been developed, few continuous processes are available [17, 22-27]:

- Wang et al. [22] used supercritical CO_2 as a solvent-free technique to physically encapsulate silica nanoparticles with Eudragit (polymethacrylate-based copolymers). Flashing the nanoparticle-polymer-supercritical CO_2 suspension from 32 °C and 8.27 MPa to ambient temperature and atmospheric pressure causes a heterogeneous polymer nucleation with the nanoparticles acting as nuclei and a subsequent growth of polymer on the surface of the nanoparticles.

- Poostforooshan et al. [23] achieved a carbon shell coating using aerosol polymerization via heterogenous condensation of both monomer and initiator on the surface of nanoparticles.

- Pfeiffer et al. [24] coated metal nanoparticles using a continuous PVD system. In this technique, an aerosol of freshly-generated core particles was passed through a metal vapor cloud, formed by spark ablation, followed by a quick quench. This causes a metal shell to quickly condense around the core particle and form a core-shell nanoparticle.

- Tavares et al [17, 25] synthesized cupper nanoparticles and functionalized their surfaces with hydrophilic and hydrophobic groups by changing the precursor gas using plasma.

- Munzer et al [26] synthesized silica nanoparticles using plasma, which were then coated via decomposition of an organic precursor (e.g. ethylene) on the surface in the afterglow heat of the plasma.

- Zhang et al [27] used photo-initiated chemical vapor deposition technique to physically coat aerosolized NaCl nanoparticles with different organic films.

Although these techniques serve as examples that free-solvent techniques can be applied for continuous, in-line processing of nanoparticles, they suffer from the use toxic materials, extreme operating conditions, complex infrastructure requirements, and high scaling costs.

To address these limitations, we built upon the principals of aerosol photopolymerization. Several studies have shown that irradiating sprayed monomer droplets with UV light leads to formation of micro- and nano-sized polymeric particles [28-30]. . This technique was subsequently refined to produce micro-scale spherical nanoparticles loaded with inorganic nanoparticles such as zinc oxide [31, 32]. . However, to the best of our knowledge, no study has reported the use of aerosol photopolymerization specifically to coat nanoparticles.

Here, we introduce a novel and simple continuous aerosol photopolymerization technique, operated at normal conditions, for in-line coating of nanopowders. To demonstrate the process, titanium dioxide nanoparticles (nano-TiO_2) and methyl methacrylate (MMA) were selected as nanoparticle and organic monomer, respectively. Nano-TiO_2 are widely used materials in industrial applications mainly as photocatalysts and reinforcers owing to their photocatalytic behavior, mechanical performance, and thermal, and optical properties [33, 34]. However, their agglomeration behavior can dramatically lower their reactivity and dispersibility in those processes [35]. Those difficulties can be overcome by coating the nanoparticles with a polymer – their inherent photocatalytic activity can be exploited in this regard to form coatings such as poly(methyl methacrylate) (PMMA), polystyrene (PS), and poly(N-isopropylacrylamide) (PNIPAM) [36].

In our previous work [37], we demonstrated a jet-impactor assisted fluidized bed (JIAFB) can break up nanoparticle agglomerates in the gas phase. While the JIAFB allowed for the production of a stream of single, de-agglomerated nanoparticles from an initially agglomerated feedstock, it did not allow the stabilization of these particle to prevent re-agglomeration. In this work, we combine JIAFB with photo-initiated chemical vapor deposition (PICVD) [1, 38, 39]. The newly de-agglomerated particles are pneumatically guided to a monomer vapor saturation zone, leading to heterogeneous condensation of the monomer onto the nanoparticles, which is subsequently photopolymerized under UV light to yield a thin carbon coating. Processing parameters are key, as photopolymerization must occur quickly before the monomer evaporates away from the surface, or re-agglomeration of nanoparticles is triggered via random collisions or liquid-bridge forces. Moreover, a thin coating (<5 nm) is desired to minimize any impact on the desirable properties of nano-TiO_2, such as its band gap.

2. Theory

2.1. Condensation of monomer vapor on nanoparticles surfaces

Condensing vapors on a particle surface is the mechanism employed by condensation particle counters (CPC), also known as a condensation nucleus counters (CNC) [40]. These are used to increase the size of fine airborne particles that are invisible to optical counters. In CPCs, fine particles pass through a saturation chamber, filled with vapors of typically lower alcohols. The vapor condenses onto the particles through heterogeneous nucleation, thereby increasing the apparent diameter of the particles as they advance through the chamber and can finally be detected by an optical counter. Here, aerosol particles act similarly as nuclei for heterogenous condensation of monomer vapors. The condensed layer grows as the particles progress through a continuous aerosol photo-reactor, and photopolymerized in flight. Thermodynamically, the probability of heterogenous condensation depends on the size of a particle, its wettability with respect to the condensing liquid, and the degree of saturation of the condensing vapor [41, 42]. If the particle is perfectly wettable, heterogenous condensation will occur for particles diameters equal or larger than the Kelvin diameter, d_k:

$$d_k = \frac{4M\sigma}{\rho RT \ln S} \tag{1}$$

where σ is the surface tension of the liquid, M is its molecular weight, ρ is its density, R is the universal gas constant, and S is the supersaturation (defined as the ratio of actual vapor pressure P in the feed to the saturation vapor pressure P_{sat} at temperature T, i.e. $S = P/P_{sat}(T)$). Accordingly, at a given S, only particles with diameters equal or larger than d_k can serve as nucleation sites for condensation (and subsequent condensational growth). Whereas heterogenous condensation will not occur for particles smaller than d_k, increasing supersaturation decreases d_k, thereby increasing the probability of condensation onto smaller particles (and the condensational growth rate). Hence, controlling the degree of saturation is important in determining d_k as well as the ultimate size of particles.

If particles are not perfectly wettable, the surface energy of the condensation process will be affected by the interaction of solid-liquid-vapor interfaces. Hence, the contact angle between the solid particle and condensing liquid governs the rate of condensation, J, [43]:

$$J = \pi d_p^2 \, 10^{25} \, exp\left(\frac{-\Delta G}{kT}\right) \tag{2}$$

where k is the Boltzman constant, T is the temperature, dp is the particle diameter, and ΔG is the energy change resulting from condensation, which is itself a function of the contact angle, θ, [44]:

$$\Delta G = \frac{16\pi\sigma^3 M^2}{3\,(\rho R T \ln S)^2} f(\theta) \tag{3}$$

These equations highlight that the stronger the vapor-particle interaction, the larger the condensation rate. Further, aerosol particles with low affinity for the condensing liquid can serve as nucleation sites for if vapor supersaturation is sufficiently high. Affinity and supersaturation will dictate whether condensation occurs film-wise or drop-wise.

To evaluate the affinity of methyl methacrylate (MMA), a liquid monomer, with the surface of nano-TiO_2 particles, contact angle goniometry tests were carried out with the sessile drop method (supplementary Fig. 1). A fine layer of nano-TiO_2 was deposited on a glass microscope slide using a high-speed air jet. The contact angle was measured using an FDS tensiometer OCA DataPhysics TBU 90E. All contact angles were recorded after five seconds from when the drop reaches the surface. The contact angle of $0°$ indicates the surface of nanopowders are perfectly wettable with MMA, which makes it suitable candidate for this experiment. While roughness effects may explain this behavior in part, the very high surface energy of nano-TiO_2 ($\sim$ 1 J/m^2) [45] compared to MMA (0.028 J/m^2) [46] is in agreement with the experimental observations.

The high wettability of MMA towards TiO_2 also allows capillary condensation to come into play. In capillary condensation, vapor condenses on the neck between neighboring particles, which leads to bridging between the particles and thus agglomeration. However, Mavliev et al. [47] have previously shown that the effect of particle charge on heterogenous condensation is insignificant for particles greater than 3 nm in diameter.
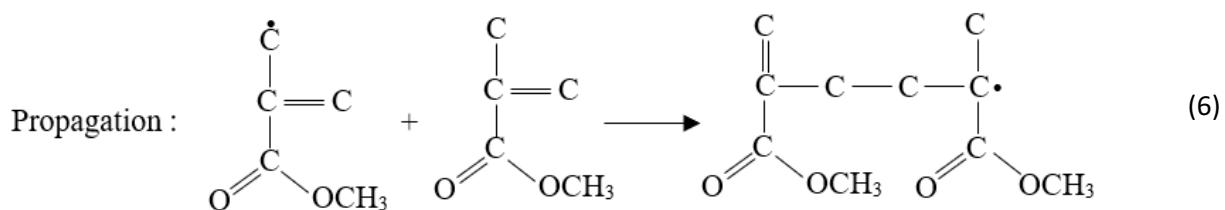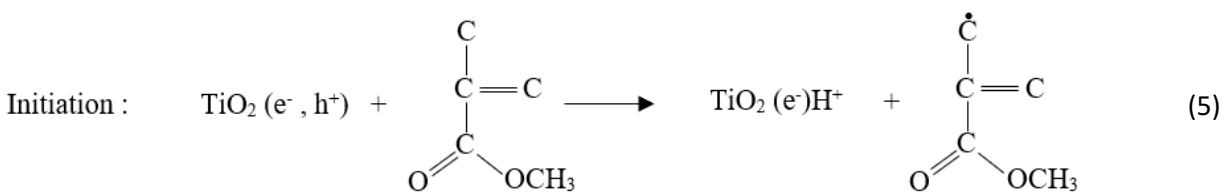
2.2. Reaction Process

Photopolymerization of MMA initiated by semiconductors (e.g. TiO_2) has been well documented [36, 48-51]. According to the UV absorption spectra of MMA, it strongly absorbs UV light below 275 nm (largely transparent at higher wavelengths) [49]. Nevertheless, the rate of MMA self-photopolymerization is low because of low monomer decomposition and radical generation rates. TiO_2 under UV light promotes radical generation, which significantly boosts the polymerization rate [49, 51]. When a TiO_2 particle is

irradiated by UV light, it generates a conduction-band electron and a valence-band hole on its surface [49]:

$$TiO_2 \xrightarrow{h\upsilon} e^-_{cb} + h^+_{vb} \tag{4}$$

Although the electrons are not strong enough to induce anionic initiation, the holes, as powerful oxidants, are capable of abstracting a hydrogen atom from the MMA monomers to generate MMA radicals. The MMA radicals, subsequently, attack other monomers and polymerization propagates through a radical polymerization:

Initiation : $TiO_2 (e^-, h^+)$ + [MMA monomer structure] ⟶ $TiO_2 (e^-)H^+$ + [MMA radical structure] (5)

Propagation : [MMA radical structure] + [MMA monomer structure] ⟶ [dimer radical structure] (6)

Since initiation originates from the surface of TiO₂, a higher particle specific surface area will lead to a faster reaction rate. TiO₂ nanoparticles lead to noticeably faster photopolymerization compared to self-polymerization of MMA [49], with the anatase phase showing a higher photoactivity than the rutile phase [52]. Akgun et al. [31] had earlier shown that MMA can be photopolymerized in the presence of nano-TiO₂ over reaction times on the order of one minute or less, in the context of polymer-matrix nanocomposite synthesis. Because the photopolymerization reaction is largely surface-initiated, this reaction scheme is pertinent to exploit in an aerosol system, given that the reaction will be selective to coating nanoparticles (no need for downstream purification to remove polymer particles). Further, a high dependency on UV radiation, as a source of energy, results in the fact that chain growth can be instantly started or stopped by turning the light on and off, respectively [53]. This offers more control on the reaction in the aerosol phase, and consequently the thickness of coating.

3. Experimental Section

3.1. Materials

Methyl methacrylate (MMA, Sigma-Aldrich, 99 % purity) was purified using a prepacked column of inhibitor remover (Sigma-Aldrich) to remove methyl hydroquinone. Titanium dioxide (anatase TiO_2, Nanostructured & Amorphous Materials, 99% purity) nanoparticles had a primary particle size of 30 nm with a specific surface area of 40-60 m^2/g and bulk density of 50 kg/m^3. Dry nitrogen (N_2, Air Liquide, 99.99% purity) was used for fluidization, jet, and carrier gas to prevent any humidity absorption by the nanopowders and undesired effects on the reaction.

3.2. Process

The experimental setup consists of three main components: a jet-impactor assisted fluidized bed (JIAFB), a monomer saturator, and a photo-reactor [Fig. 1]. The operation of the JIAFB has been fully described previously [37]. Briefly, it consists of an upward-facing micro-jet that directs fluidized nanoparticles towards an impaction plate positioned 5 mm downstream of the jet, within an 8 mm ID fluidized bed, leading to nanoparticle de-agglomeration. A venturi pump, at the outlet of the system, guides the broken agglomerates to the saturation chamber and then the photo-reactor. In the saturation chamber, monomer vapor is provided by the saturator, in which pure monomer is partially evaporated at a given temperature using a water bath (below its boiling point) and carried to the chamber by an N_2 carrier gas flow. Monomer vapor condenses onto the transported aerosol nanoparticles, which are at room temperature, in the chamber. The now-monomer-covered nanoparticles move to the photo-reactor, where they are exposed to UVC irradiation for photopolymerization. The polymer coated particles are captured downstream using an in-line filter (Whatman® Anodisc inorganic filter membranes, pore size 0.020 μm, installed inside a 47 mm stainless steel filter holder) , installed at the outlet of the photo-reactor before the venturi pump. The outlet gas flow also transits through a water trap to remove any remaining entrained particles before discharging to the ventilation system. When transmission electron microscopy (TEM) sampling is required, a rod is inserted into the photo-reactor from the top.

The photo-reactor is a cylindrical quartz tube (5 cm ID, 90 cm length) centered in a modified UV cabinet (Daavlin CO.). It is surrounded by 28 UVC fluorescent tubes (170 cm) emitting mainly at 253.7 nm with a light intensity of 0.012 W/cm^2 at a distance of 33 cm. The aerosol residence time in the saturation chamber and photo-reactor can be controlled by adjusting the inlet flows of the JIAFB (i.e. jet and fluidizing gas flows), carrier gas flow, and the pressure provided the venturi pump. In all experiments,

the flow rates of jet and carrier gases were kept constant at 0.6 and 0.5 L/min of N_2, respectively. The fluidizing gas velocity was set to 1.5 cm/s (three times larger than minimum fluidization velocity for TiO_2 nanopowder), leading to a high bed expansion and uniform fluidization of nanopowders around the micro-jet [54, 55]. Accordingly, the average residence time of the aerosol particles in the photoreactor is approximately one minute (residence time distribution obtained from two-phase simulation) .

The temperature of the saturator was set at 50 °C. At this temperature, MMA can reach an equilibrium vapor pressure of 0.15 bar. Upon subsequent cooling to room temperature, where the saturation pressure is 0.036 bar, a saturation ratio of 4.5 is achieved. This supersaturation state guarantees MMA vapor will condense on the surfaces of room-temperature particles.
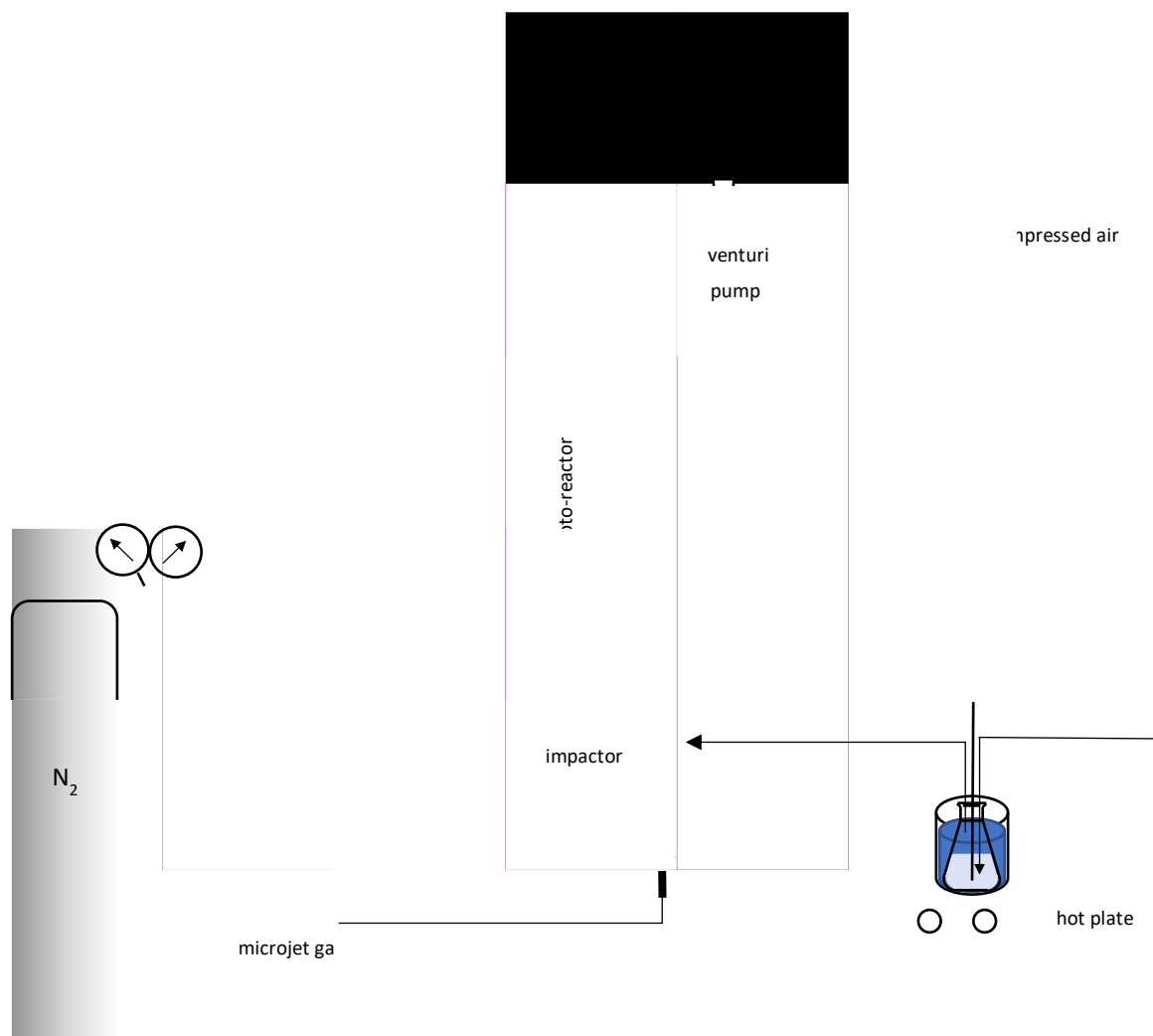

Fig. 1. Schematic diagram of the JIAFB and the continuous aerosol photo-reactor experimental set up.

3.3. Characterization Methods

TEM was carried out on a JEOL JEM-2100F operated at 200 kV in bright-field mode to confirm the presence, thickness and uniformity of the coating. The particles were deposited gently on a TEM grid (Electron Microscopy Sciences, CF-400-Cu, carbon film on a 400 square mesh copper grid) directly from the aerosol phase. ImageJ software [56] was used to determine the average thickness of coating by analyzing the thickness in five TEM micrographs.

The chemical composition of the coating was identified by Attenuated total reflectance Fourier-transform infrared spectroscopy (ATR-FTIR, Thermo Scientific Nicolet iS5 with iD7 ATR). TGA was performed in a TA Instruments Q50 apparatus at a heating rate of 10 °C/min up to 600 °C under N_2 atmosphere. Two isotherms (30 minutes each) were defined before (at 120 °C) and after (at 600°C) the ramp to remove traces of humidity or remaining monomer. The sample size was approximately 10 mg. X-ray photoelectron spectroscopy (XPS) analysis of the samples was carried out using a VG ESCALAB 3 MKII apparatus with an Mg-Kα radiation source (15 kV, 20 mA) with an aperture size of 2 × 3 mm^2. The base pressure in the UHV analysis chamber was 5 × 10^{-9} Torr and the experiments were performed at room temperature. An X-ray incident angle of 15° with a corresponding penetration depth of ~10 nm was used for survey scans. Avantage™ XPS analysis software was used to deconvolute the peaks in the high-resolution spectra. For all spectra, a classical Shirley background subtraction was used before fitting the peaks with a symmetric 50% Gauss-Lorentz sum function (0%: pure Gauss, 100%: pure Lorentz).

Particle size was measured in suspension using an Eyetech™ instrument (AmbiValue, Netherlands). This instrument measures particle size based on the theory of the Laser-Obscuration-Time, in which a single particle is scanned with a focused rotating laser beam [57]. For this purpose, a dilute suspension (0.5 g/L) of both bare and coated particles were dispersed using an ultrasonic homogenizer (Cole-Parmer, model CP505 500 W) operating at 100 W with an energy dose of 600,000 J/g$_{TiO2}$. The cuvette was filled with 3 cc of the sonicated sample immediately, followed by slow stirring to keep the particles suspended. Particle size distributions were obtained by averaging three distributions in three cycles, with each cycle lasting one minute (approximately equivalent to 5×10^6 particles measured). To quantify the dispersibility of nanopowders in different solvents, a UV-visible spectrometer (Ultrospec 1100 pro) was used to collect the absorbance spectra in the range of 200-900 nm from the same sonicated suspension.

4. Results and Discussion

4.1. Physical characterization

Bare and coated TiO_2 nanoparticles were collected directly from the aerosol phase. TEM images of the bare particles (Fig. 2.a) show agglomerated primary particles with diverse shapes in the size range of 20-40 nm. The crystallographic orientation of anatase TiO_2 can be seen at the outermost layer of the particle that clearly reveals the sharp edge of the particles. On the other hand, TEM micrographs of coated particles display a conformal thin layer of rough coating around all surfaces. Image processing demonstrates a coating thickness in the range of 0.7-3.5 nm with an average of 1.5 nm (ImageJ software). Thicker coatings were seen on the neck with neighboring particles. This can be due to the capillary condensation that causes monomer vapor condenses more on the concave surfaces rather than convex surfaces. Despite using the JIAFB upstream of the coating step, agglomeration still occurs and can be attributed to the increasing the capillary forces when nanoparticles pass through the saturator chamber. However, the coated particles agglomerates are much smaller than those observed for untreated particles (refer to section 4.3).
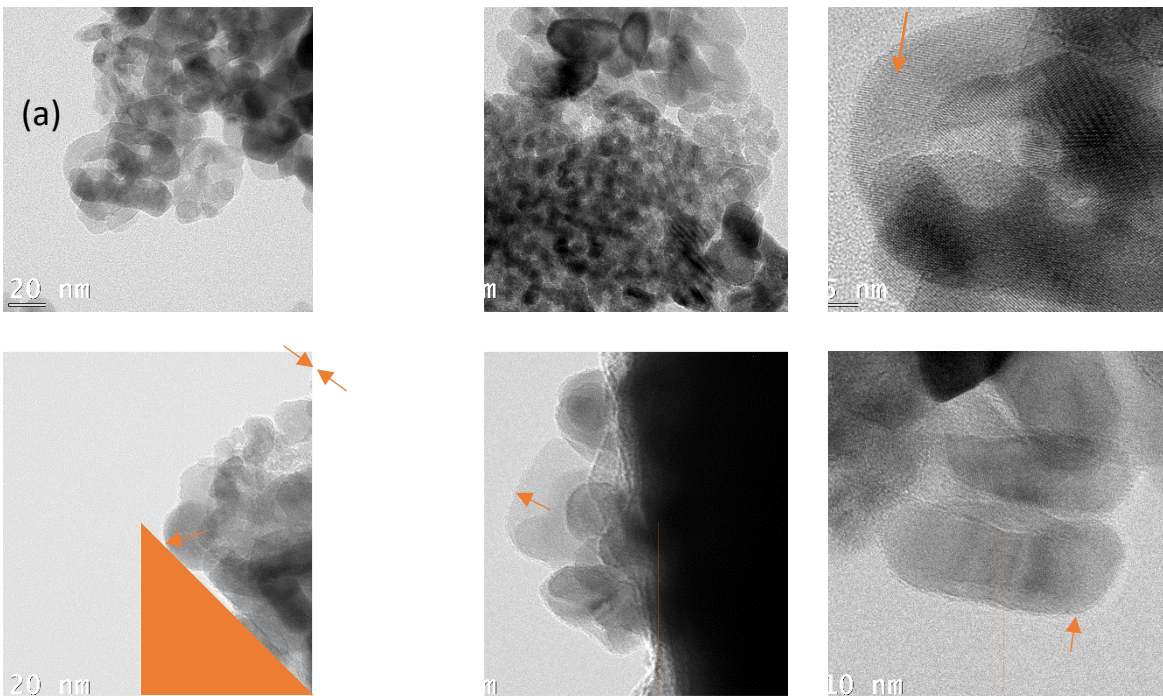

Fig. 2. TEM micrographs of (a) bare TiO2 nanoparticles and (b) coated TiO_2 nanoparticles

Thermogravimetric analysis (TGA) was carried out on the bare and coated nano-TiO$_2$ to determine the mass of the carbon film grown onto the particles (Fig. 3). Three weight loss steps can be discussed in the TGA curve: from 25 to 210 °C, both samples experience a weight loss of about 2.5% due to the adsorbed and chemisorbed humidity. This is attributed to the evaporation of non-polymerized volatile monomers that are trapped in the porosity of the coated particles. Over the 210-450 °C range, the bare particle lose 0.5% weight, while the coated particles lose approximately 3.5%. This rise in carbon content of the coated sample compared to the bare sample is ascribed to the initiation of MMA depolymerization that typically begins at around 200 °C [49, 58]. Assuming a uniform coating around nanosphere TiO$_2$, a 3% difference in weight loss is equivalent to a 1.1 nm coating around all particles, which is in agreement with the TEM results. This confirms the presence of photopolymerized MMA on the surface of nano-TiO$_2$. Above 450 °C, the bare nano-TiO$_2$ weight reduces by 1%, attributed to the loss of carbonaceous impurities from the liquid-phase TiO$_2$ synthesis process [59]. Over this same temperature range, no weight loss was observed for the coated samples.
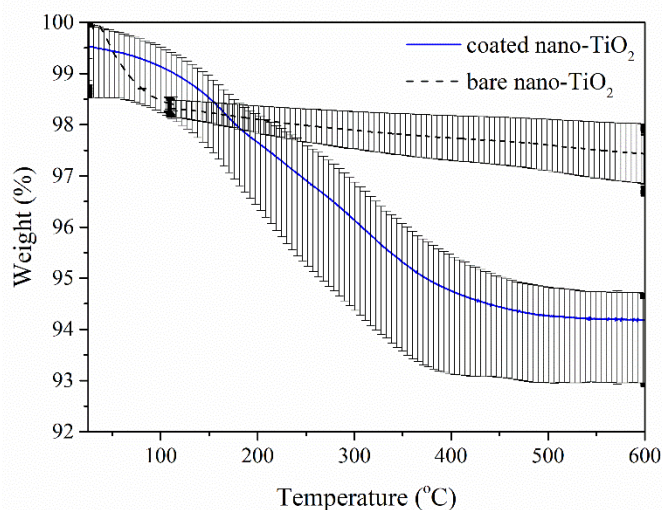

Fig. 3. TGA curves of bare and coated nano-TiO$_2$ (error bars represent standard errors of three repetitions)

4.2. Chemical characterization

The ATR-FTIR spectra of coated nano-TiO$_2$ was different from that of the untreated control sample, indicating a clear change in its surface chemical structure (Fig. 4). The sharp peak at 632 cm^{-1} in both bare and coated samples shows the stretching vibration of the Ti-O bond. In the coated sample spectrum, multiple organic peaks appear, namely at 1728 and 2950 cm^{-1} (stretching vibration of carbonyl and ester methyl C-H groups, respectively) and at 1481/1453/1438 and 1271-1063 cm^{-1} (C-H

deformations and C-O stretching, respectively). Those group of peaks are a signature of PMMA [60, 61], and are in sharp contrast to the untreated sample with no such peaks present.
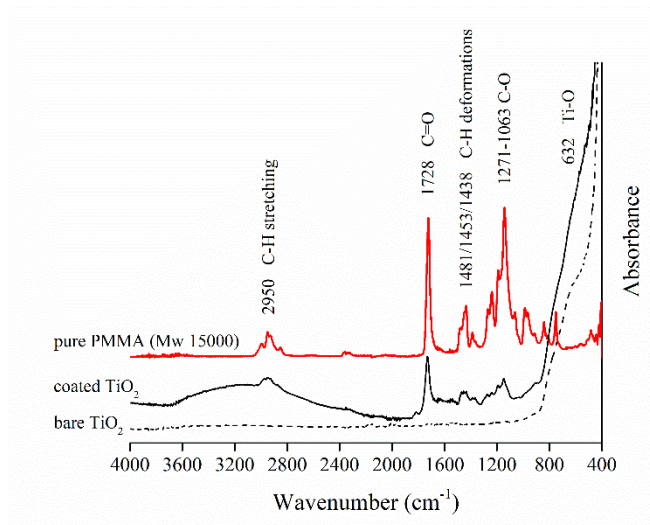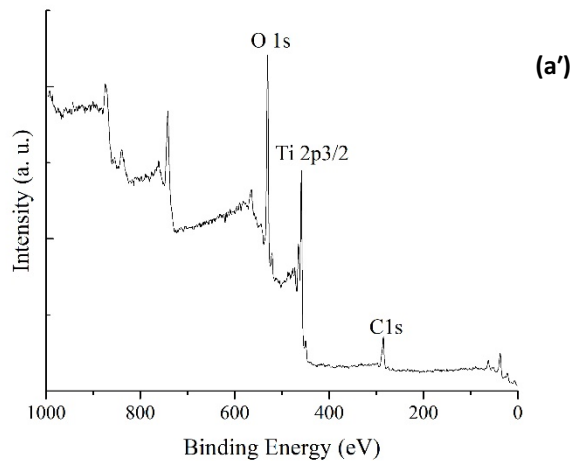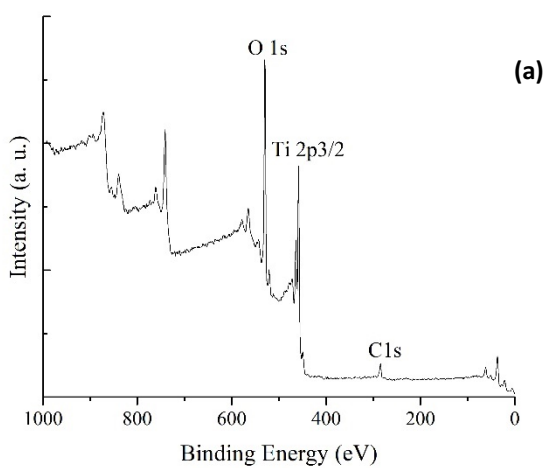

Fig. 4. IR spectra of pure PMMA (Mw 15000), bare and coated nano-TiO$_2$.
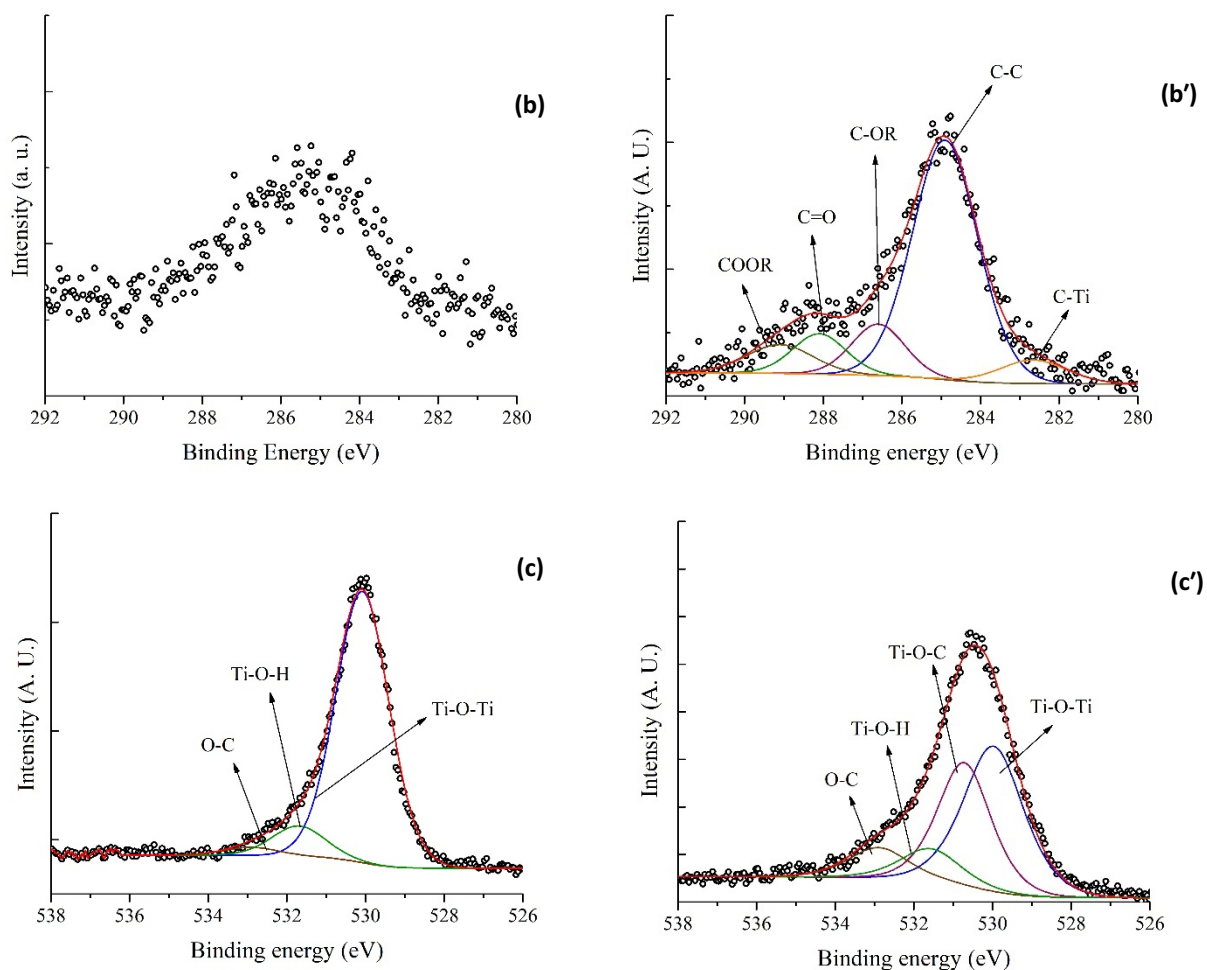
Fig. 5. XPS survey spectra of (a) bare and (a') coated nano-TiO_2; high-resolution of C 1s peak deconvolution for (b) bare and (b') coated nano-TiO_2; high-resolution of O 1s peak deconvolution for (c) bare and (c') coated nano-TiO_2

Table 1 Location of binding energies and their relative atomic % provided by high-resolution XPS (source of BE obtained by comparison of ref. [62] and [63])

Peak Name	Binding Energy (eV)	Identification	Relative atomic (%)	
			Bare	Coated
C 1s	282.5 ± 0.2	C-Ti	NA	6.5
	285.0 ± 0.2	C-C/C-H	NA	65.1
	286.5 ± 0.2	C-OH/C-OR	NA	11.4
	288.0 ± 0.2	O-C-O/C=O	NA	9.0
	289.5 ± 0.2	COOH/COOR	NA	8.0
O 1s	530.1 ± 0.2	Ti-O-Ti	87.6	45.7

530.9 ± 0.2	Ti-O-C	Not Detected	34.5
531.6 ± 0.2	Ti-O-H	9.8	10.2
532.9 ± 0.2	O-C	2.6	9.6

Quantitative XPS analysis was performed on the bare and coated samples to obtain further information of the coated film (Fig. 5, Table 1). Quantitative XPS analysis was performed on the bare and coated samples to obtain further information of the coated film (Fig. 5, Table 1), with binding energy assignments obtained from [62] and [63]. Both survey spectra show TiO$_2$'s characteristic Ti 2p and O 1s peaks (Fig. 5. a and a'), as well as a C 1s peak centered at a binding energy of 285 eV. Comparing C 1s survey peaks shows the carbon content of the coated sample is more than double that of the untreated sample, which is in agreement with the TGA analyses (minor carbon contamination in bare TiO$_2$).

Deconvolution of the C 1s and O 1s high-resolution spectra provide more detailed information about the carbon film (Fig. 5.b and b', Table 1). Unfortunately, the low signal-to-noise ratio of the bare nano-TiO$_2$ C 1s peak prohibited application of the deconvolution algorithm; this serves as additional indication that there is no carbon covalently bonded to the surface, rather it is adsorbed carbon derived from the synthesis of nanopowder. On the other hand, deconvolution of the coated sample's stronger C 1s peak showed a sub-peak centered at 282.5 eV (covalent bonding between Ti and C, 6.5 At%), and a series of sub-peaks from 285 to 289.5 eV (indicative of C-C, C-O-H, C=O, and COOH functionalities). A corresponding sub-peak in the O 1s spectrum (at 532.9 eV) confirms the presence of C-O functionalities, in-line with the previously shown IR spectrum's MMA signature [64]. The O 1s high-resolution spectrum further identifies a sub-peak at 530.9 eV, indicative of a Ti-O-C bond in the treated sample (Fig. 5.c and c'). These Ti-C and Ti-O-C covalent bonds not only shows the carbon film is grafted to the surface, but also aligns with the fact that photopolymerization is initiated from the surface of the TiO$_2$. Deconvolution of the Ti 2p peak is not presented, as the sub-peaks related to Ti-C or Ti-O-C bonds were significantly overshadowed by the peaks assigned to the substrate.

Finally, it is pertinent to note that, during XPS analysis of the coated sample, the pressure in the analysis chamber increased substantially up to 4.5×10-8 Torr upon irradiation. This typically occurs for powder samples, due to the desorption of trapped water or reagents in the porosities or adsorbed onto the surface during storage or processing [65]. This decreased to some extent the overall signal-to-noise ratio and thus the quality of the high-resolution spectra.

4.3. Particle Size Study

To examine the efficiency of de-agglomerating process, the sizes of bare and coated nano-TiO_2 were measured in n-dodecane (Fig. 6, the solvent choice is discussed further in section 4.4). Volume distribution shows a significant shift of the size of bare particles to lower sizes, despite of having an extra carbon layer on their surfaces. The average size of particles reduces from 18.25 to 1.84 μm and the particle concentrations rise from 2×10^6 to 8×10^6 #/mL. This demonstrates that the large complex agglomerates, generated during or after production, have been de-agglomerated into smaller clusters as a result of JIAFB process, and these remain small after coating and dispersion. This is mirrored by a shift of the number-based distribution average from 1.06 to 0.7 μm. It is worth mentioning that measuring particle sizes as small as the primary particle size (0.03 μm) is limited by the lower bound for detection in the instrument used (0.1 μm).
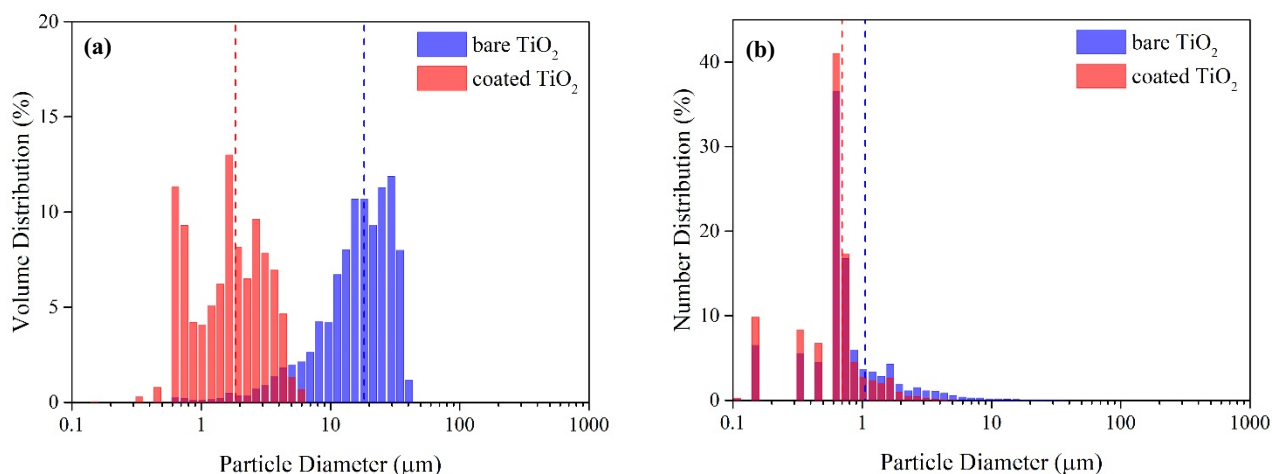

Fig. 6. Comparing particle size distributions of bare and coated nano-TiO_2 in n-dodecane in volume-based (a) and number-based distribution (b). Volume- and number-weighted mean diameters were marked as dash line on the histograms, respectively.

4.4. Dispersibility

The dispersibility of bare and coated samples in several solvents with different dielectric constants (ε) was studied qualitatively and quantitively using UV-Vis spectroscopy (Fig. 7). For this purpose, dilute (0.1 g/L) suspensions of both samples were prepared in water (polar-protic, ε = 80, relative polarity = 1), acetone (polar-aprotic, ε = 21, relative polarity = 0.35), and n-dodecane (non-polar, ε = 2, relative polarity $\cong$ 0). Nano-TiO_2, before treatment, forms a uniform and stable aqueous dispersion resulting from the hydroxyl groups on their surfaces (Fig. 7.a), but the treated particles immediately settle out of suspension given the lack of affinity of the hydrophobic MMA-based coating for the water. UV-Vis

spectra confirm this by showing a significant decrease in the absorbance of coated particle suspensions (Fig. 7.a'). Further, Christian et al. previously showed that the change of surface plasmon resonance (SPR) band can be interpreted as a change in the surface composition [66]. Accordingly, a noticeable shift of the maximum absorption wavelength (λ_{max}) from 450 to 260 nm for aqueous suspension suggests a change in the surface composition of nano-TiO$_2$. A similar behavior was observed for acetone.

In contrast, the dispersibility of bare nano-TiO$_2$ in n-dodecane was very poor (particles aggregated and sedimented immediately once mixing stopped), whereas the coated nano-TiO$_2$ exhibited an enhanced dispersion (Fig. 7.c), confirmed by the increase in the UV-Vis absorbance spectrum. This indicates a successful conversion of a hydrophilic nanoparticle to a hydrophobic particle capable of dispersion in non-polar media following treatment in the continuous aerosol photopolymerization process.
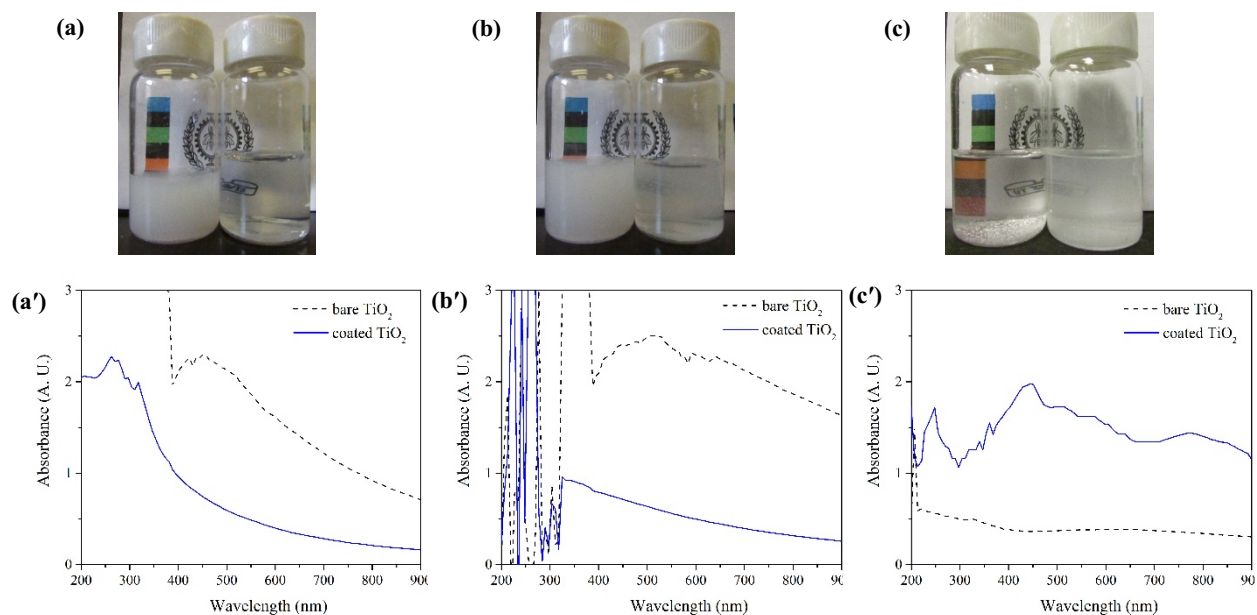

Fig. 7 Photograph and UV-Vis spectra of bare (left) and coated (right) nano-TiO2 dispersed in water (a), acetone (b), and n-dodecane (c).

To illustrate the colloidal stability of the treated particles in n-dodecane, their absorbance at 900 nm (maximum variation of light intensity) was monitored over time (every 5 min over 47 h). The treated particles show an enhanced stability of dispersion with a delayed re-agglomeration, whereas sedimentation occurs very rapidly for untreated particles (Fig. 8.a). Since the solvents are the same, the sedimentation rate of particles in the solvent depends on the physical properties (size and density) and surface-driven properties of particles (chemical affinity of particle-solvent and particle-particle). It was shown previously that the treated particles form smaller agglomerates than the bare particles (Section

4.3), which limits their settling speed. Also, the density of treated particle reduces as a result of a carbon coating. Assuming each individual particle has been coated uniformly with a 1.5 nm PMMA layer (Fig. 2), it reduces the density of bare particles by 10%. Therefore, bare particles sediment faster because they form larger and more dense agglomerates compared to the treated particles, despite their lower number concentration in solution (the higher the number concentration, the higher the agglomeration rate). According to the Hansen dispersibility theory, whenever size enlargement of particles due to agglomeration becomes important, comparing the extinction rate with respect to the relative sedimentation time (RST) is a better measurement for their stability against agglomeration/flocculation [67, 68], as RST normalizes the sedimentation time with the physical properties of the solvent:

$$RST = \frac{t(\rho_p - \rho_s)g}{\eta_s} \tag{7}$$

where ρ_p and ρ_s are the density of the particle and the solvent, respectively, η_s is the intrinsic viscosity of the solvent, and g is the acceleration of gravity. This definition is valid when the stability of a single type of particle in various solvents is going to be investigated [69]. However, when the initial particle size becomes important, the RST equation can be modified according to Stokes' sedimentation time:

$$RST = \frac{t(\rho_p - \rho_L)gr^2}{\eta_L h} \tag{8}$$

where r is the radius of the particle and h is the settling height. The RST excludes the dependency of sedimentation rate to the physical properties of the particle (e.g. particle size and density) and provides a pure measure of chemical stability of the suspension. Accordingly, the extinction profiles as a function of RST were plotted for both bare and treated particles (Fig 8.b), demonstrating that the chemical surface coating plays an important role in the suspension stability. The covalent attachment of a polymer to the particle surface enhances the stability by improving interfacial interactions [15]. Fig 8 shows the carbon coated particle not only has a lower sedimentation rate, but also causes a delayed re-agglomeration. This coating technique can be used for applications that require a good dispersibility and long-term storage in target non-polar solvents, as most of the techniques suffering from detachment of ligands from the particle surface. In addition, re-sonicating the suspension of treated particles with the same energy dose repeats this sedimentation pattern, meaning the de-agglomeration/re-agglomeration phenomenon is reversible. Also, a wide range of applications can benefit from coated nanoparticles with enhanced dispersibility in non-polar media such as reinforcing fillers in polymer matrices [70], nanofluids [71], or in high-tech electronic devices [2].
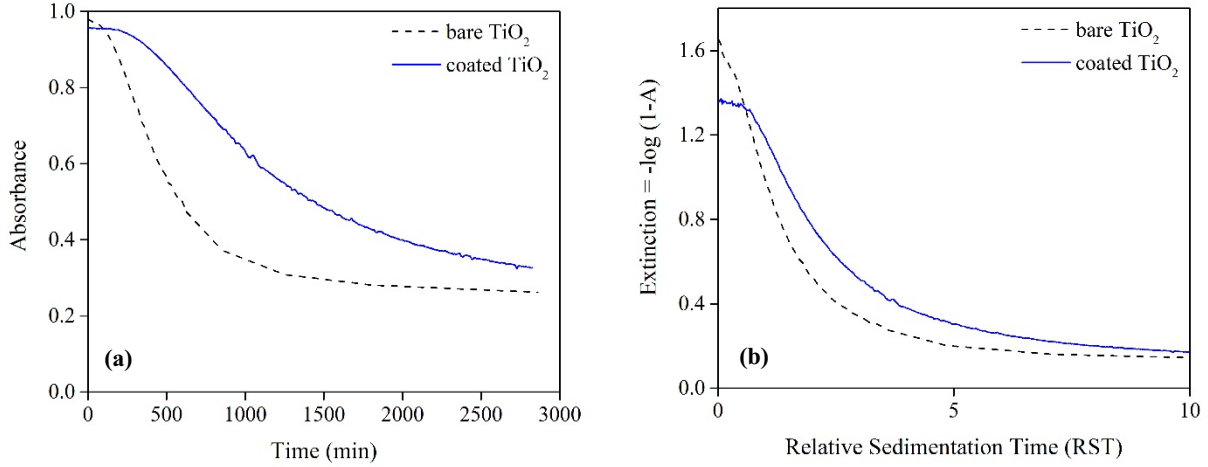
Fig. 8. (a) Absorbance of bare and coated nano-TiO₂ in n-dodecane suspension. Absorbance of 0 represent a pure n-dodecane solvent. (b) Extinction profiles of bare and coated nano-TiO₂ in n-dodecane as a function of RST.

4.5. Predicting Polymer Quantity at Different Residence Times

Before reacting, the monomer condenses on the surface through heterogeneous condensation. Hence, the particles grow by diffusion of monomer molecules from the vapor onto their surfaces. The particle growth rate at a given temperature can be estimated by using the following equation [72]:

$$r\frac{dr}{dt} = \frac{S-1}{F_k + F_d} \tag{9}$$

where, $\frac{dr}{dt}$ is the rate of increase of the radius, $F_k = \frac{L^2 \rho_l}{RKT^2}$ is a thermodynamic heat-conduction term and $F_d = \frac{\rho_l RT}{DP_s(T)}$ is a vapor diffusion term. Plotting this equation for our system (Fig. 9.a) shows that, at a saturation ratio S of 4.5, the condensation rate will be so fast that particles as small as 0.01 μm will grow to 1 μm over the first five seconds, and reach 3.5 μm after one minute. Since the final particle size distribution (Fig. 6) shows a peak particle size less than 1 μm, this means the evaporation rate is also quite fast. Given these fast evaporation and condensation rates, the reaction rate would be the limiting step that controls the final thickness of the film. MMA follows the typical kinetic rate of a free radical photopolymerization reaction [48, 49, 51, 73, 74]. Blake [73] showed that, in the absence of oxygen, the polymerization rate of MMA is first order with respect to monomer concentration and half order with respect to initiator concentration:

$$R_p = K\sqrt{C_i}C_M \tag{10}$$

where, C_i is the initiator concentration, C_M is the MMA monomer concentration, and K is the rate constant and defined by:

$$K = \sqrt{\frac{2\phi k_d}{k_t}} k_p \qquad (11)$$

in which K depends on the quantum yield of chain initiation (ϕ), and the rate constants of dissociation, polymerization, and termination reactions (k_d, k_p, k_t). At room temperature, K was evaluated as 1×10^{-4} (lit/mol)$^{0.5}$.s^{-1} for MMA free radical polymerization [73]. Assuming a reaction-limited regime (compared to condensational growth rate) allows us to predict the amount of PMMA produced during the polymerization at different residence times. In Fig. 9.b, the circular data points were measured by Fan et al. [74] for high conversions of MMA over extended periods (several hours), and show good agreement with calculations based on Equation 10. However, in the case of aerosol photopolymerization occurring over short residence times (as short as one minute, our measurement marked as square), Equation 10 significantly underestimates our experimental data. This can be due to the fact that, in aerosol photopolymerization, unlike bulk polymerization, the reaction occurs on the surface of particles. Hence, the dissociation rate, and consequently polymerization rate, in aerosol photopolymerization is significantly higher than those of bulk polymerization. Accordingly, modifying the K value to 1×10^{-2} (lit/mol)$^{0.5}$.s^{-1} to account for the increased probability of radical production and collision, Equation 10 accurately predicts the presence of PMMA (3.6%, which is comparable to the 3.5% value we reported in the TGA section, previously) (Fig 9.c). A similar approach was used by Esmaeili et al. [12] to predict the polymerization rate of ethylene when the monomer and catalysts are combined on a bed of nanopowders via condensation. In their case, the rate constant was modified by a factor of 1000.
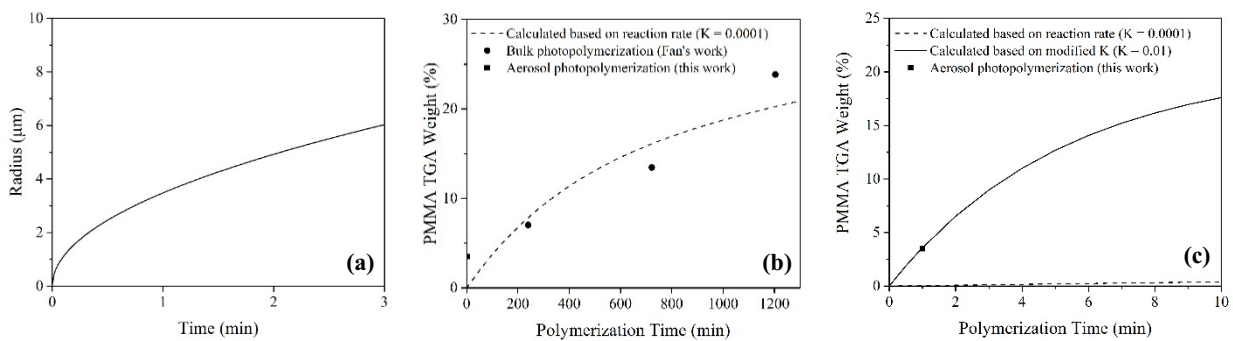
This

Fig. 9. (a) growth rate of 0.01 µm-particles in saturation ratio of 4.5 ,(b) Profile of PMMA production over time considering a first order free radical polymerization and comparing to bulk photopolymerization (measured by Fan et al [74], circles), aerosol

coating (estimated from Zhang et al [27], white squares) and this work (black square), (c) Profile of PMMA production over time with modified K

5. Conclusions

We developed a continuous aerosol photopolymerization technique to both de-agglomerate and subsequently coat TiO_2 nanoparticle with a carbon film. The MMA monomer, after heterogenous condensation on the surfaces of nanoparticles, is photopolymerized and covers the nanoparticles with a thin film. TEM images confirmed the presence of carbon coating around the nanoparticles and agglomerates in the order of 0.7 to 3.5 nm, in agreement with TGA and FTIR results. According to XPS, the film is grafted to the nano-TiO_2 surface, corroborating the fact that photopolymerization is initiated from the surface of particles. This guarantees the formation of carbon film can only happen around the particles, so that no secondary carbon-only particles can be formed during the coating process (thus maintaining sample purity).

After mixing in various solvents, UV-Vis spectroscopy illustrated the improved dispersibility of coated nano-TiO_2 in non-polar media like n-dodecane, and prevents dispersion in polar media like water or acetone. Particle size measurement confirmed that settling velocity reduces for treated particles because of lower density and smaller size of agglomerates. Further, studying the extinction rate over relative sedimentation time revealed that the polymer coating also plays an important role in stability of the suspension by providing a strong steric stabilization that results in longer term colloidal stability and delayed re-agglomeration. To control the thickness of the film, the heterogeneous condensation step will need to be refined further. Moreover, the extension of this process to other nanoparticles and polymers focus of on-going work. Although the nanoparticles were coated herein by exploiting their photo-activity, the technique can be applied to other nanopowders by using photo-active monomers, photo-initiators, or photo-sensitizers. Also, the affinity of nanopowders to polar/non-polar media can be tuned by selecting monomers that provide compatible surface groups. Coating integrity could potentially be improved by employing multifunctional acrylate monomers or adding cross-linking agents – these could increase reactivity and lead to a cross-linked outer layer. The versatility of this continuous technique, combined with the fact that it operates at ambient temperature and atmospheric pressure, is solvent-free and has low scaling costs, makes it an efficient candidate as a unit operation to be integrated into continuous aerosol nanopowders synthesis processes.

Acknowledgements

References

[1] D. Farhanian, G. De Crescenzo, J.R. Tavares, Large-Scale Encapsulation of Magnetic Iron Oxide Nanoparticles via Syngas Photo-Initiated Chemical Vapor Deposition, Sci Rep 8 (2018) 12223.

[2] B.J. Park, J.H. Sung, K.S. Kim, I. Chin, H.J. Choi, Preparation and Characterization of Poly(Methyl Methacrylate) Coated TiO2 Nanoparticles, J MACROMOL SCI B. 45 (2007) 53-60.

[3] V. Martín, R. Romero-Díez, S. Rodríguez-Rojo, M.J. Cocero, Titanium dioxide nanoparticle coating in fluidized bed via supercritical anti-solvent process (SAS), Chem. Eng. J. 279 (2015) 425-432.

[4] M. Sansotera, S. Geran Malek Kheyli, A. Baggioli, C.L. Bianchi, M.P. Pedeferri, M.V. Diamanti, W. Navarrini, Absorption and photocatalytic degradation of VOCs by perfluorinated ionomeric coating with TiO2 nanopowders for air purification, Chem. Eng. J. 361 (2019) 885-896.

[5] YupengLi, C. Zeng, C. Wang, L. Zhang, Preparation of C@silica core/shell nanoparticles from ZIF-8 for efficient ciprofloxacin adsorption, Chem. Eng. J. 343 (2018) 645-653.

[6] S. Hosseininasab, N. Faucheux, G. Soucy, J.R. Tavares, Full range of wettability through surface modification of single-wall carbon nanotubes by photo-initiated chemical vapour deposition, Chem. Eng. J. 325 (2017) 101-113.

[7] J.A.H. Lalinde, J. Jiang, G. Jai, J. Kopyscinski, Preparation and characterization of Ni/Al2O3 catalyst coatings on FeCrAl-loy plates used in a catalytic channel reactor with in-situ spatial profiling to study CO2 methanation, Chem. Eng. J. 357 (2019) 435-446.

[8] C.A. Dorval Dion, J.R. Tavares, Photo-initiated chemical vapor deposition as a scalable particle functionalization technology (a practical review), Powder Technol. 239 (2013) 484-491.

[9] V. Mirjalili, M. Yourdkhani, P. Hubert, Dispersion stability in carbon nanotube modified polymers and its effect on the fracture toughness, Nanotechnology 23 (2012) 315701.

[10] D. Wen, Y. Ding, Experimental investigation into convective heat transfer of nanofluids at the entrance region under laminar flow conditions, Int. J. Heat Mass Transfer 47 (2004) 5181-5188.

[11] J. Liu, Y. Gao, D. Cao, L. Zhang, Z. Guo, Nanoparticle dispersion and aggregation in polymer nanocomposites: insights from molecular dynamics simulation, Langmuir 27 (2011) 7926-7933.

[12] B. Esmaeili, J. Chaouki, C. Dubois, Encapsulation of nanoparticles by polymerization compounding in a gas/solid fluidized bed reactor, AIChE J. 55 (2009) 2271-2278.

[13] J. Ellison, G. Wykoff, A. Paul, R. Mohseni, A. Vasiliev, Efficient dispersion of coated silver nanoparticles in the polymer matrix, Colloids and Surfaces A: Physicochemical and Engineering Aspects 447 (2014) 67-70.

[14] F. Zhang, E. Lees, F. Amin, P. Rivera Gil, F. Yang, P. Mulvaney, W.J. Parak, Polymer-coated nanoparticles: a universal tool for biolabelling experiments, Small 7 (2011) 3113-3127.

[15] R.M. Santos, C. Vilaverde, E. Cunha, M.C. Paiva, J.A. Covas, Probing dispersion and re-agglomeration phenomena upon melt-mixing of polymer-functionalized graphite nanoplates, Soft Matter 12 (2016) 77-86.

[16] P. Rivero, J. Garcia, I. Quintana, R. Rodriguez, Design of Nanostructured Functional Coatings by Using Wet-Chemistry Methods, Coatings 8 (2018) 76.

[17] J. Tavares, E.J. Swanson, S. Coulombe, Plasma Synthesis of Coated Metal Nanoparticles with Surface Properties Tailored for Dispersion, Plasma Processes and Polymers 5 (2008) 759-769.

[18] S. Habibzadeh, O. Zabeida, A. Argoitia, R. Sargent, J. Klemberg-Sapieha, J. Chaouki, L. Martinu, Conformal Multilayer Photocatalytic Thin Films on Fine Particles by Atmospheric Pressure Fluidized Bed Chemical Vapor Deposition, Industrial & Engineering Chemistry Research 57 (2018) 10345-10353.

[19] A. Berard, G.S. Patience, G. Chouinard, J.R. Tavares, Photo Initiated Chemical Vapour Deposition To Increase Polymer Hydrophobicity, Sci Rep 6 (2016) 31574.

[20] D. Farhanian, G. De Crescenzo, J.R. Tavares, Kinetics, Chemistry, and Morphology of Syngas Photoinitiated Chemical Vapor Deposition, Langmuir 33 (2017) 1780-1791.

[21] H. Nasri Lari, D. Farhanian, D.C. Boffito, G.S. Patience, G. De Crescenzo, J. Chaouki, J.R. Tavares, Shedding light on iron pentacarbonyl photochemistry through a CVD case study, Catal. Commun. 100 (2017) 19-23.

[22] Y. Wang, R.N. Dave, R. Pfeffer, Polymer coating/encapsulation of nanoparticles using a supercritical anti-solvent process, The Journal of Supercritical Fluids 28 (2004) 85-99.

[23] J. Poostforooshan, S. Rennecke, M. Gensch, S. Beuermann, G.-P. Brunotte, G. Ziegmann, A.P. Weber, Aerosol Process for theIn SituCoating of Nanoparticles with a Polymer Shell, Aerosol Sci. Technol. 48 (2014) 1111-1122.

[24] T.V. Pfeiffer, P. Kedia, M.E. Messing, M. Valvo, A. Schmidt-Ott, Precursor-Less Coating of Nanoparticles in the Gas Phase, Materials (Basel) 8 (2015) 1027-1042.

[25] J. Tavares, S. Coulombe, Dual plasma synthesis and characterization of a stable copper–ethylene glycol nanofluid, Powder Technol. 210 (2011) 132-142.

[26] A. Münzer, J. Sellmann, P. Fortugno, A. Kempf, C. Schulz, H. Wiggers, Inline coating of silicon nanoparticles in a plasma reactor: Reactor design, simulation and experiment, Materials Today: Proceedings 4 (2017) S118-S127.

[27] B. Zhang, Y.-C. Liao, S.L. Girshick, J.T. Roberts, Growth of coatings on nanoparticles by photoinduced chemical vapor deposition, J. Nanopart. Res. 10 (2007) 173-178.

[28] R. Partch, E. Matijević, A.W. Hodgson, B.E. Aiken, Preparation of polymer colloids by chemical reactions in aerosols. I. Poly(p-tertiarybutylstyrene), Journal of Polymer Science: Polymer Chemistry Edition 21 (1983) 961-967.

[29] M. Bazzano, D. Latorre, R. Pisano, M. Sangermano, M. Woerner, Nano-structured polymeric microparticles produced via cationic aerosol photopolymerization, Journal of Photochemistry and Photobiology A: Chemistry 346 (2017) 364-371.

[30] M. Bazzano, D. Marchisio, M. Sangermano, M. Wörner, R. Pisano, A molecular dynamics approach to nanostructuring of particles produced via aerosol cationic photopolymerization, Chem. Eng. Sci. 195 (2019) 1021-1027.

[31] E. Akgün, J. Hubbuch, M. Wörner, Perspectives of aerosol-photopolymerization: organic-inorganic hybrid nanoparticles, Colloid. Polym. Sci. 292 (2014) 1241-1247.

[32] E. Akgün, A. Muntean, J. Hubbuch, M. Wörner, M. Sangermano, Cationic Aerosol Photopolymerization, Macromolecular Materials and Engineering 300 (2015) 136-139.

[33] M. Tsega, F.B. Dejene, Morphological, thermal and optical properties of TiO2 nanoparticles: The effect of titania precursor, Materials Research Express 6 (2019) 065041.

[34] Y. Zhao, C. Li, X. Liu, F. Gu, H. Jiang, W. Shao, L. Zhang, Y. He, Synthesis and optical properties of TiO2 nanoparticles, Mater. Lett. 61 (2007) 79-83.

[35] K. Suttiponparnit, J. Jiang, M. Sahu, S. Suvachittanont, T. Charinpanitkul, P. Biswas, Role of Surface Area, Primary Particle Size, and Crystal Phase on Titanium Dioxide Nanoparticle Dispersion Properties, Nanoscale Res Lett 6 (2011) 27.

[36] X. Wang, Q. Lu, X. Wang, J. Joo, M. Dahl, B. Liu, C. Gao, Y. Yin, Photocatalytic Surface-Initiated Polymerization on TiO_2 toward Well-Defined Composite Nanostructures, ACS Appl Mater Interfaces 8 (2016) 538-546.

[37] H. Nasri Lari, J. Chaouki, J.R. Tavares, De-agglomeration of nanoparticles in a jet impactor-assisted fluidized bed, Powder Technol. 316 (2017) 455-461.

[38] K. Chan, K.K. Gleason, Photoinitiated chemical vapor deposition of polymeric thin films using a volatile photoinitiator, Langmuir 21 (2005) 11773-11779.

[39] C.A. Dorval Dion, W. Raphael, E. Tong, J.R. Tavares, Photo-initiated chemical vapor deposition of thin films using syngas for the functionalization of surfaces at room temperature and near-atmospheric pressure, Surf. Coat. Technol. 244 (2014) 98-108.

[40] H.G. Merkus, Particle Size Measurements : Fundamentals, Practice, Quality, Springer Netherlands2009.

[41] C.-C. Chen, C.-J. Tao, Condensation of supersaturated water vapor on submicrometer particles of SiO_2 and TiO_2, The Journal of Chemical Physics 112 (2000) 9967-9977.

[42] V. Abdelsayed, M. Samy El-Shall, Vapor phase nucleation on neutral and charged nanoparticles: Condensation of supersaturated trifluoroethanol on Mg nanoparticles, The Journal of Chemical Physics 126 (2007) 024706.

[43] N.H. Fletcher, Size Effect in Heterogeneous Nucleation, The Journal of Chemical Physics 29 (1958) 572-576.

[44] J. Porstendörfer, H.G. Scheibel, F.G. Pohl, O. Preining, G. Reischl, P.E. Wagner, Heterogeneous Nucleation of Water Vapor on Monodispersed Ag and NaCl Particles with Diameters Between 6 and 18 nm, Aerosol Sci. Technol. 4 (2007) 65-79.

[45] P.A. Bhatt, S. Mishra, P.K. Jha, A. Pratap, Size-dependent surface energy and Tolman length of TiO_2 and SnO_2 nanoparticles, Physica B: Condensed Matter 461 (2015) 101-105.

[46] C. Bruel, S. Queffeulou, T. Darlow, N. Virgilio, J.R. Tavares, G.S. Patience, Experimental methods in chemical engineering: Contact angles, The Canadian Journal of Chemical Engineering 97 (2019) 832-842.

[47] R. Mavliev, P.K. Hopke, H.-C. Wang, D.-W. Lee, A Transition from Heterogeneous to Homogeneous Nucleation in the Turbulent Mixing CNC, Aerosol Sci. Technol. 35 (2001) 586-595.

[48] A.J. Hoffman, H. Yee, G. Mills, M.R. Hoffmann, Photoinitiated polymerization of methyl methacrylate using Q-sized zinc oxide colloids, The Journal of Physical Chemistry 96 (1992) 5540-5546.

[49] C. Dong, X.Y. Ni, The photopolymerization and characterization of methyl methacrylate initiated by nanosized titanium dioxide, Journal of Macromolecular Science-Pure and Applied Chemistry A41 (2004) 547-563.

[50] C.G. I. Sideridou-Karayannidou , O. Orfanou , G. Seretoudi & A. Varvoglis, Photopolymerization of Methyl Methacrylate and other Acrylates with the Use of [Hydroxy(tosyloxy)iodo]benzene as Photoinitiator, Journal of Macromolecular Science-Pure and Applied Chemistry 30 (1993) 781-788.

[51] B. Kraeutler, H. Reiche, A.J. Bard, R.G. Hocker, Initiation of free radical polymerization by heterogeneous photocatalysis at semiconductor powders, Journal of Polymer Science: Polymer Letters Edition 17 (1979) 535-538.

[52] T. Luttrell, S. Halpegamage, J. Tao, A. Kramer, E. Sutter, M. Batzill, Why is anatase a better photocatalyst than rutile?--Model studies on epitaxial TiO_2 films, Sci Rep 4 (2014) 4043.

[53] M. Chen, M. Zhong, J.A. Johnson, Light-Controlled Radical Polymerization: Mechanisms, Methods, and Applications, Chem. Rev. 116 (2016) 10167-10211.

[54] D.M.K. J. Ruud van Ommen, Alan Weimer, Robert Pfeffer, Berend van Wachem, Experiments and modelling of micro-jet assisted fluidization of nanoparticles, (2010).

[55] R.P.J.A.Q.J. Flesch, Fluidized bed systems and methods including micro-jet flow, in: U. Patent (Ed.), Orion Engineered Carbons GmbH New Jersey Institute of Technology, US, 2012.

[56] C.A. Schneider, W.S. Rasband, K.W. Eliceiri, NIH Image to ImageJ: 25 years of image analysis, Nature Methods 9 (2012) 671-675.

[57] EyeTech™ Application Note 2017.01: Particle size analysis related to dissolution and crystallisation studies, February 2020.

[58] J.R. MacCallum, The thermal degradation of poly(methyl methacrylate), Die Makromolekulare Chemie 83 (1965) 137-147.

[59] S. Gupta, M. Tripathi, A review on the synthesis of TiO2 nanoparticles by solution route, Open Chemistry 10 (2012).

[60] www.webbook.nist.gov, 2019.

[61] M. Penescu, Diffusion of cyclic versus linear poly(oxyethylene) oligomers in poly(methyl methacrylate) by atr - ftir spectroscopy, Chemistry and Biochemistry, Georgia Institute of Technology, Georgia Institute of Technology, August 2009.

[62] J.F. Moulder, Handbook of X-ray Photoelectron Spectroscopy: A Reference Book of Standard Spectra for Identification and Interpretation of XPS Data, illustrated ed., Physical Electronics Division, Perkin-Elmer Corporation, 19921992.

[63] S. Umrao, S. Abraham, F. Theil, S. Pandey, V. Ciobota, P.K. Shukla, C.J. Rupp, S. Chakraborty, R. Ahuja, J. Popp, B. Dietzek, A. Srivastava, A possible mechanism for the emergence of an additional band gap due to a Ti–O–C bond in the TiO2–graphene hybrid system for enhanced photodegradation of methylene blue under visible light, RSC Adv. 4 (2014) 59890-59901.

[64] G. Beamson, A. Bunn, D. Briggs, High-resolution monochromated XPS of poly(methyl methacrylate) thin films on a conducting substrate, Surf. Interface Anal. 17 (1991) 105-115.

[65] P. Krishnan, M. Liu, P.A. Itty, Z. Liu, V. Rheinheimer, M.H. Zhang, P.J. Monteiro, L.E. Yu, Characterization of photocatalytic TiO2 powder under varied environments using near ambient pressure X-ray photoelectron spectroscopy, Sci Rep 7 (2017) 43298.

[66] P. Christian, M. Bromfield, Preparation of small silver, gold and coppernanoparticles which disperse in both polar and non-polar solvents, J. Mater. Chem. 20 (2010) 1135-1139.

[67] C.M. Hansen, Hansen Solubility Parameters: A User's Handbook, CRC Press, Boca Raton, Fla, 2000.

[68] C. Bruel, J.R. Tavares, P.J. Carreau, M.C. Heuzey, The structural amphiphilicity of cellulosenanocrystals characterized from their cohesion parameters, Carbohydr. Polym. 205 (2019) 184-191.

[69] S. Süß, T. Sobisch, W. Peukert, D. Lerche, D. Segets, Determination of Hansen parameters for particles: A standardized routine based on analytical centrifugation, Adv. Powder Technol. 29 (2018) 1550-1561.

[70] G.W.B.E. T. J. Pinnavaia (Editor), Polymer-Clay Nanocomposites, Chichester: Wiley.2001.

[71] R. Taylor, S. Coulombe, T. Otanicar, P. Phelan, A. Gunawan, W. Lv, G. Rosengarten, R. Prasher, H. Tyagi, Small particles, big impacts: A review of the diverse applications of nanofluids, J. Appl. Phys. 113 (2013) 011301.

[72] C.D. O'Dowd, P.E. Wagner, Nucleation and Atmospheric Aerosols: 17th International Conference, Galway, Ireland, 2007, Springer2007.

[73] S.T. BALKE, The free radical polymerization of methyl methacrylate to high conversions, Faculty of Graduate Studies, McMaster University, 1972.

[74] X. Fan, L. Lin, P.B. Messersmith, Surface-initiated polymerization from TiO2 nanoparticle surfaces through a biomimetic initiator: A new route toward polymer–matrix nanocomposites, Compos. Sci. Technol. 66 (2006) 1198-1204.